nature nanotechnology

ARTICLES

PUBLISHED ONLINE: 21 JUNE 2009 | DOI: 10.1038/NNANO.2009.152

Towards single-molecule nanomechanical mass spectrometry

A. K. Naik[1†], M. S. Hanay[1†], W. K. Hiebert[1,2†], X. L. Feng[1] and M. L. Roukes[1*]

Mass spectrometry provides rapid and quantitative identification of protein species with relatively low sample consumption. The trend towards biological analysis at increasingly smaller scales, ultimately down to the volume of an individual cell, continues, and mass spectrometry with a sensitivity of a few to single molecules will be necessary. Nanoelectromechanical systems provide unparalleled mass sensitivity, which is now sufficient for the detection of individual molecular species in real time. Here, we report the first demonstration of mass spectrometry based on single biological molecule detection with a nanoelectromechanical system. In our nanoelectromechanical–mass spectrometry system, nanoparticles and protein species are introduced by electrospray injection from the fluid phase in ambient conditions into vacuum, and are subsequently delivered to the nanoelectromechanical system detector by hexapole ion optics. Precipitous frequency shifts, proportional to the mass, are recorded in real time as analytes adsorb, one by one, onto a phase-locked, ultrahigh-frequency nanoelectromechanical resonator. These first nanoelectromechanical system–mass spectrometry spectra, obtained with modest mass sensitivity from only several hundred mass adsorption events, presage the future capabilities of this approach. We also outline the substantial improvements that are feasible in the near term, some of which are unique to nanoelectromechanical system based-mass spectrometry.

Nanoelectromechanical systems (NEMS)[1] are enabling important emerging applications in diverse fields ranging from quantum measurement to biotechnology[2–9]. In general, the smaller a device, the more susceptible are its physical properties to perturbation by external influences. This enhanced sensitivity of NEMS is opening a variety of unprecedented opportunities for applications such as mass spectrometry, which is now widely used for proteomics[10,11]. Furthermore, to reliably detect the expression of low-level signals and to understand the fundamental biological processes, it is important to develop techniques capable of single-cell or single-molecule analyses[12,13]. In this work, the exceptional mass sensitivity of ultrahigh-frequency (UHF) NEMS resonators[14–18]—derived from their miniscule masses, high frequencies, and high resonance quality factors—is used to demonstrate a new paradigm for mass spectrometry. Our approach enables the first real-time detection of individual protein molecules and nanoparticles as they adsorb on a sensitive NEMS detector. We use these to carry out an initial form of mass spectrometry based on discrete adsorption events.

The vibrational frequency of a NEMS resonator is an exquisitely sensitive function of its total mass. Small variations in mass, for example, from adsorbed addenda, can measurably alter its resonant frequency. Theoretical calculations for physically realizable devices indicate that NEMS mass sensitivity below a single dalton (1 Da = 1 AMU) is achievable[19,20]. Experimental measurements of NEMS mass sensing at the ~1,000 Da level[17,21] and, more recently, below the 200 Da level[22,23] have been demonstrated. Our NEMS–MS (mass spectrometry) paradigm is also quite distinct from existing approaches to mass spectrometry in that the inertial mass of each arriving species—atom, molecule or nanoparticle—is 'weighed' as the analyte adsorbs upon the detector. Hence, a mass analyser is not needed to pre-separate and aggregate similar species. In fact, it is possible to contemplate circumventing analyte ionization entirely if alternative injection and transport methods for neutral species are used. This may offer significant advantages for whole-protein MS of high-mass species by circumventing electrostatic fragmentation. It should also dramatically reduce analyte consumption by permitting the mass detector to be positioned in close proximity to the protein source. The singular advantage of NEMS–MS is that each NEMS sensor in the single-molecule limit acts as an individual mass spectrometer. This NEMS-based mass spectrometry system, combined with other micro- and nanoscale technology[24,25], offers the possibility of compact, massively parallel MS, limited only by the number of NEMS mass sensors incorporated on a chip.

NEMS-based mass spectrometry

Typically, mass spectrometers comprise three separate components that provide the critical functions of operation: analyte ionization, analyte separation and detection. Analyte species in the fluid phase are first ionized, and bare (unsolvated) ions are produced using electrospray ionization (ESI)[26,27]. Second, ion separation is undertaken in vacuum based on the charge-to-mass (m/z) ratio of the analytes. Third, detection of clustered groups of these analytes with similar m/z values is carried out to determine the presence of a given species. Our new paradigm of NEMS–MS combines the latter two functions into one: the NEMS sensor is used as both mass analyser and mass detector. This NEMS mass analyser/detector, in this first realization described here, is preceded by well-validated mass spectrometry components for analyte injection and delivery. Figure 1 schematically depicts our prototype experimental system, which introduces, transports and measures the masses of analytes. Protein ions or charged nanoparticles are produced and stripped of fluidic solvent in the course of ESI. These bare ions traverse through a three-stage differentially pumped vacuum system and land onto the NEMS mass analyser/detector situated ~2 m away from the ESI source. Two stages of hexapole ion optics[28] driven at radio frequency (an RF-only hexapole) are used to guide the species to the NEMS with minimal m/z discrimination, as desired (see Supplementary Information). As the individual protein molecules and nanoparticles arrive and accrete onto the NEMS

[1]Kavli Nanoscience Institute, California Institute of Technology, MC 114-36, Pasadena, California 91125, USA, [2]National Institute for Nanotechnology, National Research Council of Canada, Edmonton, Alberta T6G 2M9, Canada; †These authors contributed equally to this work. *e-mail: roukes@caltech.edu

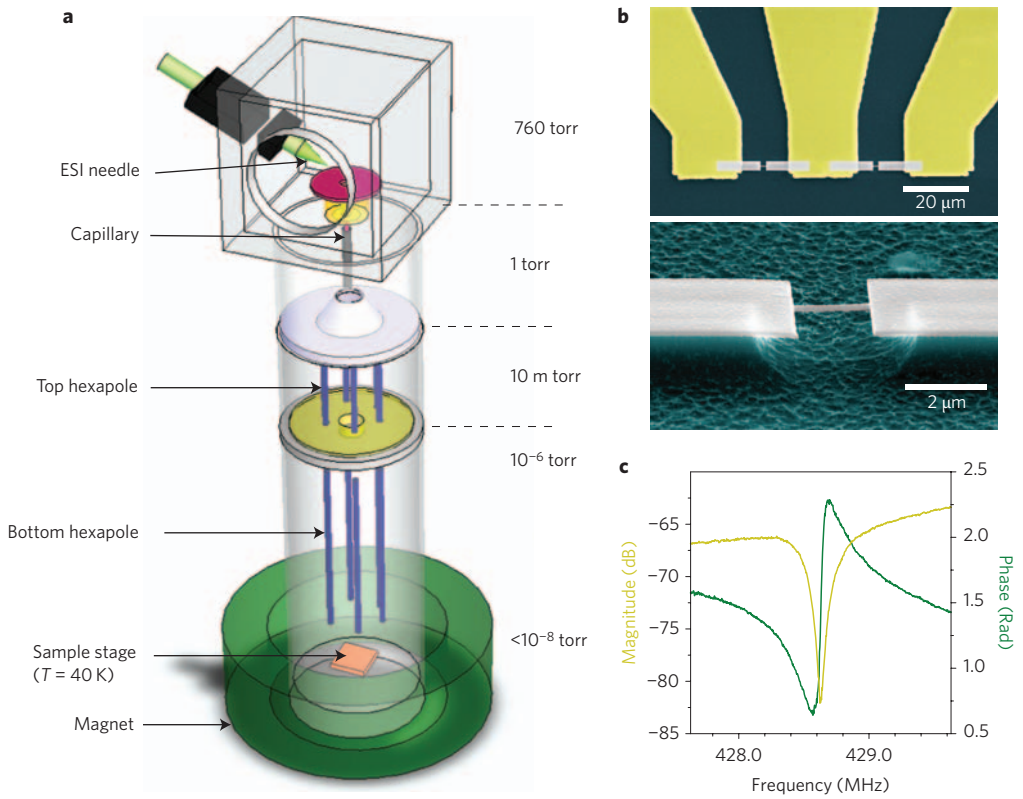

Figure 1 | First-generation NEMS–MS system. a, Simplified schematic of the experimental configuration (not to scale), showing the fluid-phase electrospray ionization (ESI) and injection, the system's three-stage differential pumping and its two-stage ion optics. **b**, Scanning electron micrographs showing one of the doubly clamped beam NEMS devices used in these experiments. It is embedded in a nanofabricated three-terminal UHF bridge circuit. **c**, Magnitude and phase of the UHF NEMS resonator's response displaying a prominent fundamental-mode resonance near 428 MHz.

sensor, its resonant frequency jumps downward abruptly with each individual molecular or nanoparticle adsorption event (Fig. 2). These precipitous events, which are absent during the control runs (see Supplementary information), are the hallmark of NEMS mass sensing with single-molecule (-nanoparticle) sensitivity. They are observed here directly for the first time, and are the centrepiece of this work.

Each quasi-instantaneous frequency jump provides information about the specific atom, molecule or nanoparticle that has just adsorbed onto the sensor. The jump height for each event—that is, the resonator's adsorbate-induced frequency deviation—depends upon both the mass of the arriving analyte and its position of adsorption on the NEMS resonator. This response is characterized by a position-dependent mass responsivity for the NEMS resonator (see Supplementary information).

Single-molecule event analysis

There are two ways through which we can extract the adsorbate mass from the convolved mass- and position-dependence of these adsorption-induced jumps. The more difficult to achieve, but conceptually most transparent, is to orchestrate simultaneous measurement of both jump height and landing position for each species as it arrives, in real time. We shall return to discuss this option below. For our first proof-of-principle demonstration reported here, we take a second, simpler approach—that of building histograms of event probability versus frequency-shift amplitude for small ensembles of sequential single-molecule or single-nanoparticle adsorption events. Figure 3a shows event probabilities calculated for sequential adsorption events originating from a monodisperse source of nanoparticles and their subsequent measurement by a NEMS detector. We assume the resonant mass detector to be a doubly clamped beam operating in fundamental mode, as in our experiments, and we scale the results to correspond both to our experimentally established NEMS mass responsivity and the masses of the gold nanoparticles we have used, which have a nominal ~2.5 nm radius. Figure 3a shows both the ideal case (zero nanoparticle size dispersion and perfect mass sensitivity) as well as more realistic experimental situations that include both the effects of finite size dispersion and the detector's frequency-fluctuation noise. Together, these latter effects reduce the resolution available in a practical system. It is readily apparent from Fig. 3 that the 'canonical' event-probability response is bicuspid, with cusps near zero and at a specific, maximum frequency shift that is associated with adsorption events at the central, most sensitive region of the beam vibrating in fundamental mode. Below, we shall use this characteristic fundamental-mode event-probability shape function to achieve mass analysis in these first NEMS–MS efforts.

NEMS–MS spectra

We report here the first NEMS–MS spectra for proteins and nanoparticles. Our analyses are carried out by observing, for each species introduced by electrospray, several hundred discrete and abrupt frequency shifts in real time—each associated with an individual protein or nanoparticle adsorption event. Each ESI run is followed by a control run of equal duration, during which the ESI solution pump is shut off to establish the frequency-fluctuation background (see Supplementary information). Given the ~250 Hz resolution in these measurements, we construct event probability histograms with 250 Hz bins and reject false positives arising from frequency-fluctuation noise by discarding jumps smaller than 2σ (= 500 Hz).

Figure 3b shows an experimental histogram constructed from data obtained by electrospraying a colloidal solution of gold nanoparticles (see Supplementary information). The gold nanoparticles

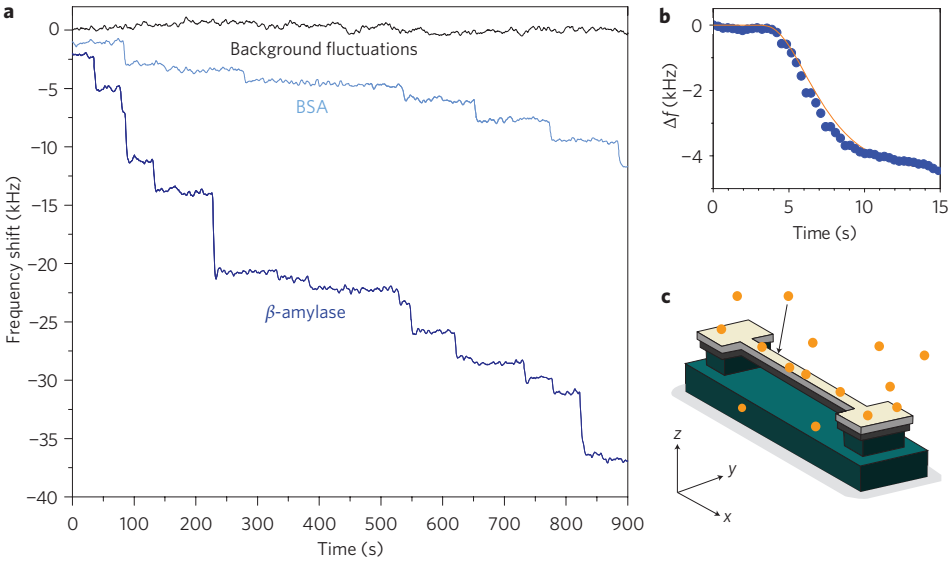

Figure 2 | Real-time records of single-molecule adsorption events on a NEMS mass sensor. a, These raw experimental data show the distinctly different, precipitous resonance frequency shifts of the NEMS during ESI-induced adsorption of BSA (66 kDa) and β-amylase (200 kDa). Each frequency jump downward is due to an individual protein adsorption event on the NEMS mass sensor. The height of each frequency jump is a convolved function of the mass of the protein that has adsorbed, and its position of adsorption upon the NEMS. **b**, Raw data from a typical discrete event (blue dots), and a nonlinear least-squares fit to the system's response (orange line), based on the temporal response function of the control loop. **c**, Schematic illustrating single-molecule adsorption events on a NEMS resonator, and the coordinate system used to define its position-dependent mass responsivity. The device itself comprises silicon carbide (dark grey) with a metallic layer (light grey) on top. The silicon substrate (green) beneath the silicon carbide is etched to release (suspend) the doubly clamped beam. The molecules are shown in orange.

used are characterized by the vendor as having an average radius of 2.5 nm and standard deviation of 'less than' 0.375 nm (Sigma-Aldrich). What is ostensibly a small standard deviation in radius actually corresponds to a rather large spread in nanoparticle mass; the advertised specifications translate to an average mass of ~780 kDa and 1σ mass range of 480–1,190 kDa. This substantial dispersion and our finite frequency-fluctuation noise together result in significant smoothing of the canonical bicuspid spectrum expected for the ideal case (Fig. 3a).

The inset to Fig. 3b shows the residues for a two-parameter least-squares fit of a theoretical event-probability curve to the experimental histogram data. The two fitting parameters are average nanoparticle radius and its dispersion; the theoretical curve incorporates the experimentally measured frequency shift resolution of $\delta f \approx 250$ Hz. With this approach, by recording just 544 individual nanoparticle adsorption events, we resolve an average nanoparticle radius of 2.15 nm, corresponding to an average mass of 490 kDa, with a standard deviation of nanoparticle radius of 0.5 nm.

Figure 4 shows NEMS–MS spectra obtained for a 'nominally pure' solution of the protein bovine serum albumin (BSA, 66 kDa) (see Supplementary information). From the standpoint of MS, pure solutions of protein are the exception rather than the rule[29,30], and the NEMS–MS spectra of Fig. 4 bear out this truism. Protein molecules often aggregate in solution to form oligomers (see Supplementary information), and each distinct molecular assemblage present in the sample will produce its own characteristic bicuspid NEMS–MS histogram. A multicomponent solution of such oligomers will thus superpose to produce a complex spectrum.

The presence of a family of oligomers has two significant effects on the shape of NEMS–MS histograms. First, the low-frequency shift cusps for each of the oligomers (occurring at the same, zero, frequency shift) superpose to produce a single, prominent peak. Second, the high-frequency shift cusps of the oligomers, which occur at different frequency shifts corresponding to each specific component's mass, become engulfed in the tails from other components. This tends to suppress their overall individual prominence. Figure 4 illustrates event probabilities as a function of frequency shift for electrosprayed BSA ions that are transported to the NEMS sensor with a hexapole drive frequency of 1.1 MHz. For comparison, also shown are theoretically expected event probabilities for BSA oligomers, generated using the experimentally measured NEMS sensor's mass responsivity of ~12 Hz zg^{-1} and using a least-squares fit to the data—similar to that used for the gold nanoparticle dispersion, but here implemented to extract the spectral weights for the first five oligomers (see Supplementary information). The spectrum in Fig. 4 shows clear peaks at 3,375 and 5,875 Hz, assigned to BSA trimers and pentamers, respectively. The broadly distributed spectral weight below 2 kHz arises from monomers and dimers. Note that this full spectrum has been obtained by recording the individual adsorption of only 578 BSA molecules.

Prospects for NEMS–MS

We believe these initial results demonstrate the potential of NEMS for MS and provide an unequivocal proof-of-principle for real-time detection of individual proteins and nanoparticles. The full capabilities and sensitivity of the new NEMS–MS paradigm will unfold in a second-generation realization providing both mass- and position-sensing in real time, for each analyte molecule as it arrives. This approach will completely obviate the need for the histogram-based analyses used in the first demonstrations reported here.

The procedure for simultaneous mass and position sensing exists[31,32], and has been experimentally proven at the microscale[31]. In automated, real-time form, it involves the simultaneous excitation, frequency-locking and tracking of multiple vibrational modes of the resonant NEMS mass sensor. As each analyte adsorbs onto the sensor, it induces a distinct frequency shift for each of the modes monitored. The combined information from the time-correlated shifts from just two modes provides sufficient information to deconvolve the adsorbate's mass and position for each event as it occurs. Tracking additional modes over-determines the solution, providing reduced variance in the deduced values of

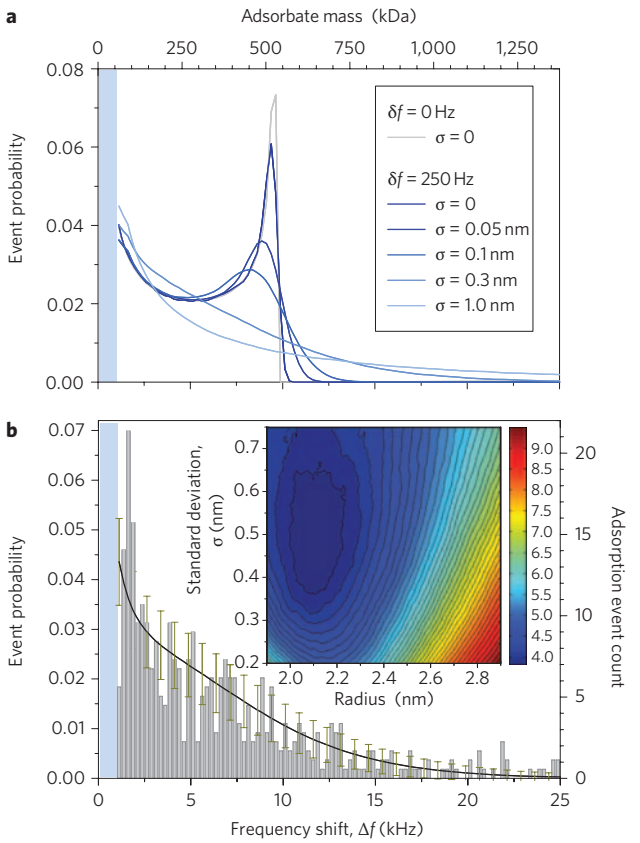

Figure 3 | NEMS mass spectrometry of a gold nanoparticle dispersion. a, Theoretically expected event probabilities versus frequency-jump amplitudes are shown for 'nominal' 2.5-nm-radius gold nanoparticles (modelled assuming a 2.15 nm mean radius), delivered with an average flux that is uniformly distributed over a doubly clamped beam having peak mass responsivity of ~12 Hz zg^{-1}. The traces show the expected results for a monodisperse ensemble of particles for the cases of perfect (0 Hz) and experimentally relevant (250 Hz) frequency resolutions, and also for several dispersions (characterized by their radius standard deviations) at 250 Hz. **b**, Experimentally obtained histogram of adsorption event probabilities versus frequency-jump amplitude for electrosprayed gold nanoparticles, and the expected curve for an average radius of 2.15 nm and a radial dispersion of 0.375 nm (black trace). The error bars display the theoretically expected deviations corresponding to 544 adsorption events, as registered in this experiment. Inset: contour plot showing the residues for least-squares fits to the experimental data using radius and radial dispersion as the fitting parameter. These data establish the average radius and size dispersion for the 544 nanoparticles measured.

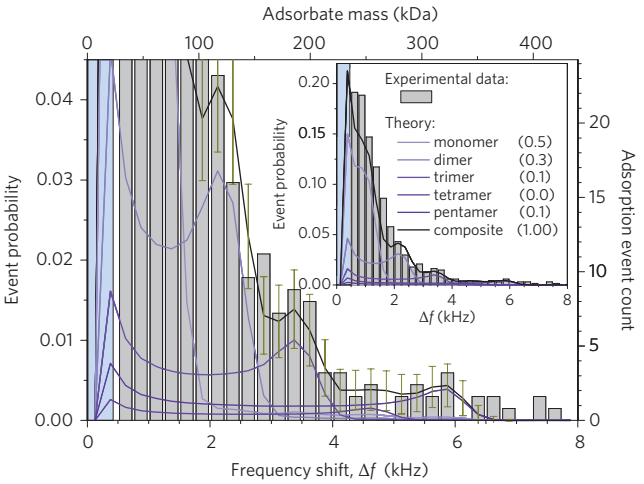

Figure 4 | NEMS–MS of proteins. NEMS–MS of BSA enabled by adsorption-event probability analysis. Experimentally obtained frequency-jump data are binned into 250 Hz histograms commensurate with the experimental mass sensitivity. Applying a 2σ detection criterion, we reject data below 500 Hz (blue-shaded regions; see text). The main plot shows an expanded view of the low-event-probability region, displaying a clearly detailed decomposition of the simultaneous contributions from oligomers. The theoretical composite curve (grey) is a weighted superposition of adsorption probabilities of the intact monomer and a family of its oligomers deterministically calculated by a least-squares process similar to that of Fig. 3 (see also Supplementary information). The inset shows the entire dataset for the 578 BSA molecular adsorption events recorded in this experiment. The numerically determined best-fit weighting coefficients for the composite curve are displayed.

particle mass and position of adsorption. This added technological component will permit the mass of each arriving molecule to be quantitatively measured in real time as it adsorbs upon the NEMS, down to the sensitivity limit imposed by the mass noise floor.

We outline below the anticipated capabilities of NEMS–MS vis-à-vis other current techniques.

Mass resolution. Mass resolution in current implementations of MS is typically defined as the ratio of the mass/charge (m/z) value and the width of the mass peaks at half maxima. The best mass resolution is obtained with Fourier transform mass spectrometry (FTMS) systems, which attain mass resolutions of the order of 2,000,000, with typical measurement times of about a second. The resolution in FTMS is high at low m/z, but deteriorates with higher m/z. Unlike the current MS systems, which measure the mass-to-charge ratio, NEMS devices measure the mass of the molecule directly. Achieving a mass sensitivity of 1 Da with a NEMS device[20] will provide the ability to distinguish two species differing by a single Da. For a 1 kDa molecule, this would be equivalent to a mass resolution of 1,000; however, NEMS–MS is capable of measuring molecules greatly exceeding 1 MDa, which means state-of-the-art mass resolution is attainable. With longer measurement times the mass sensitivity can be further enhanced. The upper limit of the mass sensitivity is set by noise sources such as $1/f$ fluctuations and long-term drifts, which always become predominant at long measurement times. The state-of-the-art of mass sensing with NEMS devices has been improving roughly by about an order of magnitude per year for the last several years; the current record is approaching 100 Da (refs 14, 15, 17, 22, 23). The ultimate limits imposed by thermodynamically driven fluctuation processes have also been theoretically established to be comfortably below 1 Da (refs 19 and 20) for measurement times in the ten millisecond range.

Mass accuracy. Mass accuracy is the ability of the instrument to accurately establish the absolute m/z (mass in NEMS–MS) of the species and is usually expressed in parts per million. A NEMS device with single dalton mass sensitivity, calibrated with an appropriate mass standard, will have a mass accuracy of 100 ppm for a 10 kDa molecule. In NEMS–MS the accuracy increases in direct proportion to the mass of the analyte molecule.

Mass or m/z range. NEMS devices have an exceptionally large mass dynamic range. These devices can easily measure biomolecules with masses of tens of MDa and still be sensitive enough to detect mass changes of a single dalton. The upper limit on the mass is set by the mass of the NEMS device itself. Depending upon the details of adsorption, the properties of the NEMS become affected only when the mass accreted becomes comparable to that of the device itself.

This translates into an upper mass limit of hundreds of MDa for typical devices[15,20]. The lower mass limit in the case of detection of large biomolecules may ultimately become limited by the spatial extent of the molecule compared to that of the NEMS sensor.

Scan speed. NEMS devices, in principle, are capable of mass sensitivities of a single dalton for measurement (integration) times in the tens of milliseconds range. Additionally, in future NEMS–MS systems, species of all m/z or masses will be measured simultaneously using arrays of NEMS devices.

Efficiency of protein transport from the source to the NEMS detector. As mentioned, the NEMS–MS system combines the role of analyser and detector into a single unit. This enables a significant reduction in the distance between the protein source and the detector, and thus a corresponding improvement in the efficiency of transport and capture. In the so-called nanoESI–MS systems, for instance, efficiencies as high as 10% have been observed[33]. Loss of analyte molecules arises from a combination of factors such as incomplete desolvation, transmission losses through the ion optics and detection inefficiency. We anticipate that future NEMS–MS systems will be based upon arrays of NEMS devices to provide maximal capture efficiency.

Parallel processing of the mass information. In NEMS-based MS systems each NEMS device acts as an individual mass sensor. Here, the capture cross-sectional area has dimensions of approximately 100 nm × 1,000 nm. This small cross-section has implications for the parallel-processing abilities of such a system. In 100 s, a modest NEMS–MS system consisting of 1,000 devices could quantitatively process 1,000 × 100 molecules s^{-1} × 100 s = 10 million molecules. Integration densities that greatly exceed this have already been realized[34]. This throughput should be sufficient for intensive analyses, for example, on individual mammalian cells.

Enhancing NEMS–MS efficiency

Transitioning previous demonstrations of NEMS mass sensing, carried out under controlled laboratory conditions, into practical and useful realizations of NEMS-based biological and chemical mass spectrometry—with the potential to process thousands of proteins in tens of milliseconds using only picolitres of sample—will require surmounting challenges in nanoscale systems integration. In future implementations, analytes must be delivered from aqueous phase, stripped of solvent, then delivered to and captured with high efficiency by the NEMS sensor. More challenging will be attaining high capture efficiency; this necessitates a mass detector with large capture cross-section. Given the size of nanoscale detectors, this will be possible only through the use of large sensor arrays positioned in relatively close proximity to the analyte injection point. This will require practical routes to very large-scale integration of NEMS. It is also clearly essential to increase sample throughput in future-generation NEMS–MS systems. The NEMS–MS paradigm is exceptionally well suited to these ends; highly multiplexed configurations involving, potentially, thousands of injectors and detectors can each be co-integrated with microfluidic pre-analysis and delivery components to create a system capable of efficiently analysing extremely small total volumes down to that of an individual cell. For the foreseeable future, we believe that the recent advances in top-down wafer-scale nanofabrication processes provide the only viable avenue to the requisite level of systems complexity. Accordingly, our current work towards the advancement of NEMS–MS is focused upon NEMS arrays fabricated in this manner[34].

Methods

Protein/nanoparticle detection and frequency jump extraction. To accommodate the stochastic sequential arrival of individual protein molecules or nanoparticles we automate our real-time analysis process. This involves two separate procedures. First, we continuously track resonant frequency in real time, using a low-noise UHF phase-locked loop (PLL) while protein ions or charged nanoparticles are injected by electrospray and delivered to the NEMS sensor by the ion optics. Figure 2 shows a typical experimental time record of the changes in resonant frequency of a phase-locked NEMS mass sensor under such conditions. Note, that each abrupt frequency jump downwards is the result of a single protein molecule or nanoparticle landing on the NEMS mass sensor. Second, we automate the numerical extraction of the jump heights (frequency shifts) for each individual adsorption event observed in these time records. Our procedure is to reject jumps smaller than twice the frequency resolution of the phase-locked NEMS sensor, because any such smaller events will be increasingly biased by false counts associated with the 'noise floor' set by the frequency instability of the phase-locked NEMS resonator. In our current measurements this instability is characterized by a typical Allan deviation of $\sigma_A(\tau) \approx 2 \times 10^{-7}$, for measurement integration times τ of the order of several seconds. This corresponds to a one-standard-deviation frequency resolution of $\delta f \approx 250$ Hz and mass noise floor of ~10 kDa in the experiments (see Supplementary information). For the remaining events, identified by our automated and unbiased numerical procedure as experimentally significant ($\Delta f \geq 2 \times \delta f$), we extract their corresponding jump heights (frequency shifts). This involves fitting the time record of each jump to the known temporal step-response function for our phase-locked NEMS system using a nonlinear least-square fit. The response function is separately calculated by PLL circuit theory, and has been experimentally verified, separately, for each NEMS mass sensor used in this work.

Physisorption. To ensure stable adsorption and immobilization of individual proteins on the NEMS detector, the detector stage is maintained at a temperature of ~40 K *in vacuo*. At reduced temperature, physisorption due to van der Waals forces ensures the proteins or nanoparticles adsorb and become immobilized upon the detector's surface. Note that detector cooling is required primarily for stable protein adsorption, not for enhanced noise performance. Physisorption is also an ideal method for analyte immobilization in that it is non-specific and it enables detector 'recycling' by periodically warming the NEMS sensor to desorb accreted species.

Measurement electronics. The detection circuitry uses a bridge circuit to null the UHF background near the NEMS resonance[14,16–18] and a frequency-modulated PLL (FM–PLL) to track the NEMS resonant frequency in real time[15]. For the very low particle flux used in this initial work, a PLL time constant of several seconds ensures each abrupt frequency jump event is recorded with many data points (Fig. 2). We determine the temporal stability of the PLL system and characterize the frequency-fluctuation noise background by operating in phase-lock over extended intervals (≫1,000 s), both with and without the activation of ESI.

We also monitor the ion current reaching the detector stage with a Faraday cup placed in close proximity to the NEMS detector, which is connected to a high-resolution electrometer. In this first-generation prototype, we do not attempt to demonstrate the potential of high-throughput NEMS–MS; the present system configuration provides a conveniently infrequent analyte arrival rate at the NEMS sensor. A typical current of ~1 pA observed at the Faraday detector yields about two adsorption events per minute.

Received 6 February 2009; accepted 14 May 2009;
published online 21 June 2009

References

1. Roukes, M. L. Nanoelectromechanical systems face the future. *Phys. World* **14,** 25–31 (February 2001).
2. Naik, A. *et al.* Cooling a nanomechanical resonator with quantum back-action. *Nature* **443,** 193–196 (2006).
3. Burg, T. P. & Manalis, S. R. Suspended microchannel resonators for biomolecular detection. *Appl. Phys. Lett.* **83,** 2698–2700 (2003).
4. LaHaye, M. D., Buu, O., Camarota, B. & Schwab, K. C. Approaching the quantum limit of a nanomechanical resonator. *Science* **304,** 74–77 (2004).
5. Thompson, J. D. *et al.* Strong dispersive coupling of a high-finesse cavity to a micromechanical membrane. *Nature* **452,** 72–75 (2008).
6. Rugar, D., Budakian, R., Mamin, H. J. & Chui, B. W. Single spin detection by magnetic resonance force microscopy. *Nature* **430,** 329–332 (2004).
7. Schwab, K., Henriksen, E. A., Worlock, J. M. & Roukes, M. L. Measurement of the quantum of thermal conductance. *Nature* **404,** 974–977 (2000).
8. Burg, T. P. *et al.* Weighing of biomolecules, single cells and single nanoparticles in fluid. *Nature* **446,** 1066–1069 (2007).
9. Ilic, B., Yang, Y. & Craighead, H. G. Virus detection using nanoelectromechanical devices. *Appl. Phys. Lett.* **85,** 2604–2606 (2004).
10. Domon, B. & Aebersold, R. Mass spectrometry and protein analysis. *Science* **312,** 212–217 (2006).
11. Aebersold, R. & Mann, M. Mass spectrometry-based proteomics. *Nature* **422,** 198–207 (2003).
12. Yu, J., Xiao, J., Ren, X., Lao, K. & Xie, X. S. Probing gene expression in live cells, one protein molecule at a time. *Science* **311,** 1600–1603 (2006).
13. Cai, L., Friedman, N. & Xie, X. S. Stochastic protein expression in individual cells at the single molecule level. *Nature* **440,** 358–362 (2006).

14. Ekinci, K. L., Huang, X. M. H. & Roukes, M. L. Ultrasensitive nanoelectromechanical mass detection. *Appl. Phys. Lett.* **84,** 4469–4471 (2004).
15. Yang, Y. T., Callegari, C., Feng, X. L., Ekinci, K. L. & Roukes, M. L. Zeptogram-scale nanomechanical mass sensing. *Nano Lett.* **6,** 583–586 (2006).
16. Feng, X. L., White, C. J., Hajimiri, A. & Roukes, M. L. A self-sustaining ultrahigh-frequency nanoelectromechanical oscillator. *Nature Nanotech.* **3,** 342–346 (2008).
17. Feng, X. L. *Ultra high frequency nanoelectromechanical systems with low noise technologies for single molecule mass sensing.* PhD. thesis, California Institute of Technology (2006).
18. Roukes, M. L. & Ekinci, K. L. Apparatus and method for ultrasensitive nanoelectromechanical mass detection. US patent 6,722,200 (2004).
19. Cleland, A. N. Thermomechanical noise limits on parametric sensing with nanomechanical resonators. *New J. Phys.* **7,** 235 (2005).
20. Ekinci, K. L., Yang, Y. T. & Roukes, M. L. Ultimate limits to inertial mass sensing based upon nanoelectromechanical systems. *J. Appl. Phys.* **95,** 2682–2689 (2004).
21. Lassagne, B., Garcia-Sanchez, D., Aguasca, A. & Bachtold, A. Ultrasensitive mass sensing with a nanotube electromechanical resonator. *Nano Lett.* **8,** 3735–3738 (2008).
22. Jensen, K., Kim, K. & Zettl, A. An atomic-resolution nanomechanical mass sensor. *Nature Nanotech.* **3,** 533–537 (2008).
23. Chiu, H.-Y., Hung, P., Postma, H. W. C. & Bockrath, M. Atomic-scale mass sensing using carbon nanotube resonators. *Nano Lett.* **8,** 4342–4346 (2008).
24. Blain, M. G. *et al.* Towards the hand-held mass spectrometer: design considerations, simulation and fabrication of micrometer-scaled cylindrical ion traps. *Int. J. Mass Spectrom.* **236,** 91–104 (2004).
25. Xie, J., Miao, Y., Shih, J., Tai, Y. C. & Lee, T. D. Microfluidic platform for liquid chromatography-tandem mass spectrometry analyses of complex peptide mixtures. *Anal. Chem.* **77,** 6947–6953 (2005).
26. Yamashita, M. & Fenn, J. B. Electrospray ion source. Another variation on the free-jet theme. *J. Phys. Chem.* **88,** 4451–4459 (1984).
27. Fenn, J. B., Mann, M., Meng, C. K., Wong, S. F. & Whitehouse, C. M. Electrospray ionization for mass spectrometry of large biomolecules. *Science* **246,** 64–71 (1989).
28. Dieter, G. Inhomogeneous RF fields: A versatile tool for the study of processes with slow ions, in *Advances in Chemical Physics: State-Selected and State-To-State Ion-Molecule Reaction Dynamics* (eds Ng, C. Y., Baer, M., Prigogine, I. & Rice, S. A.) 1–176 (Wiley, 2007).
29. Heck, A. J. & van den Heuvel, R. H. H. Investigation of intact protein complexes by mass spectrometry. *Mass Spectrom. Rev.* **23,** 368–389 (2004).
30. van Berkel, W. J., van den Heuvel, R. H., Versluis, C. & Heck, A. J. Detection of intact megadalton protein assemblies of vanillyl-alcohol oxidase by mass spectrometry. *Protein Sci.* **9,** 435–439 (2000).
31. Dohn, S., Svendsen, W., Boisen, A. & Hansen, O. Mass and position determination of attached particles on cantilever based mass sensors. *Rev. Sci. Instrum.* **78,** 103303 (2007).
32. Hanay, M. S. & Roukes, M. L. Multimode detection schemes for NEMS-based mass spectrometry. US patent CIT-4423-P (2005).
33. El-Faramawy, A., Siu, K. W. M. & Thomson, B. A. Efficiency of nano-electrospray ionization. *J. Am. Soc. Mass. Spectrom.* **16,** 1702–1707 (2005).
34. http://www.nanovlsi.org.

Acknowledgements

We acknowledge support from the NIH under grant R21-GM072898 and, indirectly, from DARPA/MTO under DOI/NBCH1050001 (MGA program) and SPAWAR/N66001-02-1-8914 (CSAC program). The latter has enabled development of critical NEMS technology for this work. We thank S. Stryker for expert technical assistance in constructing the NEMS-MS system, C. A. Zorman and M. Mehregany for custom SiC epilayers used in our NEMS fabrication, V. Semenchenko, D. A. Van Valen and R. Philips for help with gel electrophoresis, and I. Bargatin, J. L. Beauchamp, W. Lee, E. B. Myers and M. Shahgoli for helpful discussions.

Author contributions

A.K.N. and M.S.H. fabricated devices, performed experiments, analysed results and carried out some simulations. W.K.H. designed and assembled the system and performed the initial experiments. X.L.F. made the devices and did the initial phase-locked loop measurements. M.L.R. conceived the project and provided overall guidance throughout. All authors discussed the results and were involved in the analyses and manuscript preparation.

Additional information

Supplementary information accompanies this paper at www.nature.com/naturenanotechnology. Reprints and permission information is available online at http://npg.nature.com/reprintsandpermissions/. Correspondence and requests for materials should be addressed to M.L.R.

nature nanotechnology

SUPPLEMENTARY INFORMATION

DOI: 10.1038/NNANO.2009.152

Towards single-molecule nanomechanical mass spectrometry

A. K. Naik*[1], M. S. Hanay*[1], W. K. Hiebert*[1,2], X. L. Feng[1], M. L. Roukes†[1]

[1] *Kavli Nanoscience Institute, California Institute of Technology, MC 114-36, Pasadena, CA 91125 USA*

[2] *National Institute for Nanotechnology, National Research Council of Canada, Edmonton, Alberta T6G 2M9 Canada*

NEMS-MS System Overview

We employ proven methodologies from state-of-the-art mass spectrometry to build a novel MS system using ultra high frequency NEMS mass sensors. Components include a room-temperature, atmospheric pressure electrospray ionization (ESI) system for creating protein ions or charged nanoparticles, a two-stage differential vacuum system, RF hexapole ion optics to guide the charged analytes to the detector, and the NEMS mass detector stage. These are assembled to form a hybrid system comprising both custom built and commercial instrumentation.

Figure S1 is a montage of images depicting our first experimental prototype system for NEMS-MS enabling the introduction, transport, and mass measurements on individual proteins and nanoparticles. Protein ions or charged nanoparticles are produced using electrospray ionization (ESI) and delivered to a hexapole ion guide driven at radio frequencies (RF), which then transports these species to the NEMS mass sensor with minimal *m/z* discrimination, as desired. The detection circuitry utilizes a bridge circuit to null the background near the NEMS

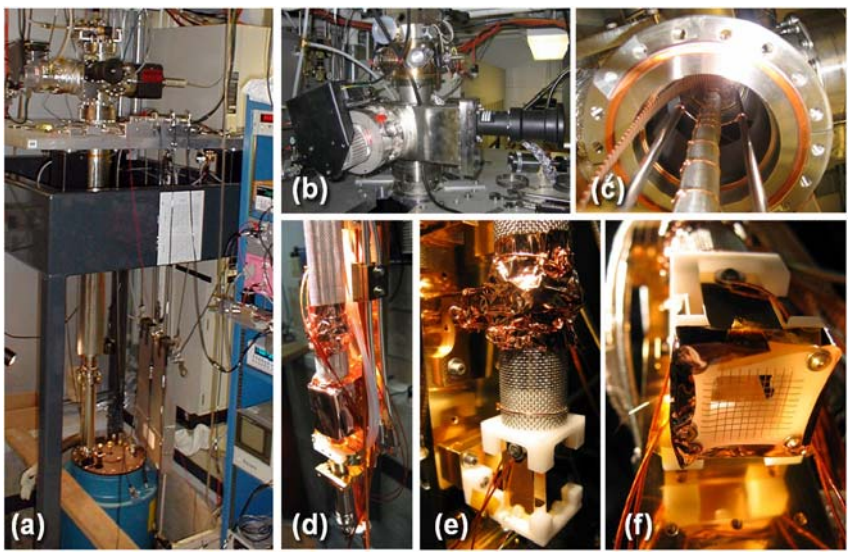

Figure S1. First Generation NEMS-MS System. *(a) The cryostat, its vibration isolation & support system, and (in pit) the super-conducting magnet, and its dewar. (b) Electrospray ioniza-tion unit at top of system. (c) Hexapole ion guide from bottom. (d)(e) Sample stage region; progres-sive magnifications. (f) Hexapole ion guide; outlet detail.*

*These authors contributed equally to this work.

DOI: 10.1038/NNANO.2009.152

resonance[1-3] and a frequency-modulated, phase-locked loop (FM-PLL) to track the NEMS resonant frequency in real time[4].

Biological sample preparation

Bovine Serum Albumin (BSA), β-Amylase and 5-nm (nominal) diameter colloidal gold nanoparticles were obtained from Sigma-Aldrich and used without further purification. The solutions employed for ESI are as follows:

1. Bovine Serum Albumin (Mol. Wt.=66kDa) : 25 μM solution in 95/5 v% H_2O/HAc
2. β-Amylase (Mol. Wt.=200kDa) : 0.2 μM in pH~6.5 10mM NH_4Ac buffer in 50/50 v% H_2O/MeOH
3. Sigma-Aldrich colloidal gold nanoparticle solution (G1402) diluted ten-fold by 50/50 v% H_2O/MeOH

Electrospray Injection (ESI) and differential vacuum assembly

Protein ions and charged nanoparticles are produced using a commercial electrospray ionization (ESI) system (Varian). ESI is one of two well known "soft" ionization processes that can reliably bring large macromolecules from the solution phase into the vapor phase[5,6].

These solutions were introduced using a syringe pump (Harvard Apparatus) and syringes (Hamilton) to the electrospray needle (Agilent) by direct infusion through standard MS components (Upchurch) to achieve typical flow rates of 4 μL/min. High-voltage sources (Emco) are used to bias the ESI needle at a constant voltage of ~2.5-3kV. Solvated analytes delivered to the needle are forced out in the form of charged droplets that repel each other due to coulombic forces[5,6]. The solvent within these droplets evaporates, reducing their volume yet preserving the amount of charge contained. The increasingly unstable microdroplets eventually undergo "coulomb fission", fragmenting into daughter droplets, and repeated cycles of this process ultimately result in the formation of bare ionized proteins. Although the exact mechanism of protein ion formation from small droplets is still under debate[7], electrospray has become a well-established technique for producing proteins in vapor form.

Our ESI delivery system is built around a commercial sub-assembly (Varian 1200 LC/MS) and comprises the following components:

1) An ESI needle and gas sheath mounted in an outer chamber at atmospheric pressure and room temperature.

2) A 1st vacuum stage with a shield plate, counterflow gas path, capillary, and pumping port.

3) A 2nd vacuum stage including a skimmer, collisional-cooling hexapole ("top hexapole"), and final high vacuum orifice. This sub-assembly is embedded in a custom 2nd stage vacuum chamber designed for about 10 mTorr base pressure for optimal collisional cooling[8,9] of the ions. It is then attached to the top plate of the high-vacuum cryostat chamber housing the "bottom hexapole" (see below) and the NEMS sample stage.

All N_2 gas, vacuum port, electronic, and fluidic lines are connected to external instrumentation.

† Corresponding author: roukes@caltech.edu

Ion transport

Electrospray ionization is typically performed at atmospheric pressure and at room, or elevated, temperature. This enables the solvent droplets that form beyond the Taylor cone to quickly evaporate leaving the bare protein ions they contain. In this first-generation NEMS-MS realization we employ physisorption to capture and immobilize the analytes on the NEMS sensor's surface. By contrast, this requires that the NEMS be maintained under high-vacuum and low temperature conditions. Our experimental setup must therefore provide a match between these rather different conditions; we achieve this with a combination of commercially-available and custom-built cryogenic and differential-pumping components. In our first-generation design the NEMS sample stage is located about 2m away from the ESI source. Since the capture area of the NEMS sensor is small, this necessitates efficient transport of the analyte ions created by electrospray to guide them along a 2m path to the surface of the NEMS sensor for adsorption.

Transport of ions from atmospheric pressure to the first differential pumping stage is performed through the so called nozzle-skimmer configuration[10,11]. This produces a highly collinear, monochromatic beam of nitrogen molecules and protein ions. Subsequently, the ions are transported from this initial vacuum stage to the NEMS sensor by a hexapole ion guide system, having an outer radius of ~ 1.2 cm and total length of ~ 2m. The hexapole configuration was chosen as a good compromise between obtaining high transmission efficiency and providing

Parameter	Description	Typical Values
V_{needle}	Voltage on the electrospray needle	3.0kV
V_{L4}	Voltage on the electrostatic lens between top and bottom hexapole	-20V
V_{shield}	Voltage on the shield (ESI counter electrode)	600V
$V_{capillary}$	Voltage on the capillary	200V
V_{top_hex}	DC offset voltage on the top hexapole	10V
V_{bot_hex}	DC offset voltage on the bottom hexapole	0V
f_{RF}	RF frequency of AC voltage applied to the hexapole	1.1MHz, 450kHz
V_{RF}	Amplitude of the RF voltage applied to hexapole	500V
P_{int}	Pressure in the intermediate collisional focusing chamber	8mTorr
T_{dry}	Temperature of the drying gas	180^0C
P_{dry}	Pressure of the drying gas	30psi
P_{neb}	Pressure of the nebulising gas	15psi
R	Protein solution flow rate	4μl/min

Table I. *Typical values used during ESI and ion optics*

DOI: 10.1038/NNANO.2009.152

minimal *m/z* selectivity, to permit simultaneous and non-discriminative transport of a broad range of bio-/chemical species. The configuration we employ actually involves two independent hexapole ion guide stages. The top hexapole, operating in the 10 mTorr vacuum range, provides collisional cooling and trapping of the ions and relies on space charge for injection through an orifice into the vacuum chamber of the main cryostat. The bottom hexapole operating in high vacuum plays a dual role. It acts as an ion "pipe", enabling broadband, high-efficiency transmission of ions over the 2m path. It is also key in overcoming the magnetic mirror effect that would otherwise reflect the ions back along their initial path as they tried to enter the high magnetic field region[12,13]. (As described below, we have employed well-validated magnetomotive displacement transduction for the NEMS in this first generation system; it provides optimal sensitivity in a high magnetic field.) Both hexapoles are driven by a homemade RF oscillator [14,15] that can supply AC voltages of up to $500V_{peak}$. In brief, the RF power supply is based on two vacuum tubes operating in a push-pull oscillator configuration, driving an LC load formed by the capacitive load of the hexapole rods and high-voltage inductor and capacitors to tune to the frequency of oscillation. The significant length of the lower hexapole sets an upper limit to the frequency that can effectively be applied by the voltage source, though this upper limit did not come into play for the large mass species probed in this experiment. The NEMS mass sensor is centered about 3mm below the bottom end of the hexapole guide.

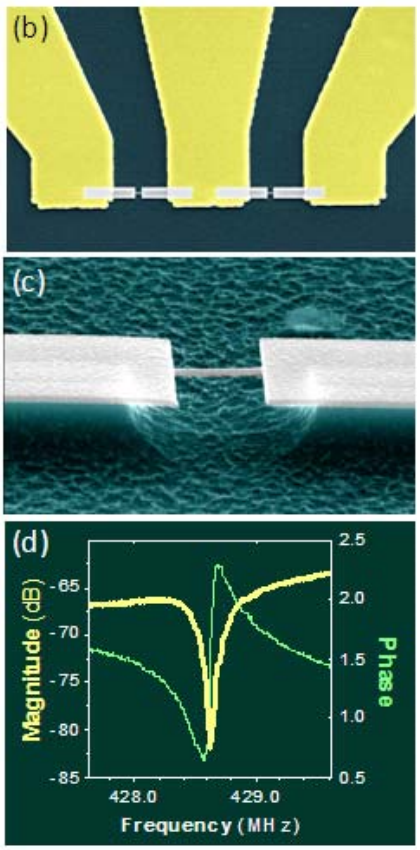

Figure S2. *(From Figure 1 of main paper)* ***(a,b)*** *Scanning electron micrographs showing one of the NEMS device used in the experiments.* ***(c)*** *Magnitude and phase of the UHF NEMS resonator's response displaying a fundamental mode resonance near 429MHz.*

NEMS Device Fabrication

The structural material for the ultrahigh frequency (UHF) NEMS devices in this work is a 100nm thick single crystal 3-C silicon carbide (SiC) epilayer deposited on a silicon substrate through molecular beam epitaxy[16]. Thin-film metal conductors are defined by optical lithography to form wirebond pads and a lead-frame that converges into the central, active region of each device where the NEMS are located. Each of these small chips is manually diced for subsequent individual processing. Electron-beam lithography is used to laterally define what ultimately become nanometer-scale NEMS features on the SiC epilayer. Thermal evaporation is used to deposit 40nm of Al followed by 5nm Ti on these patterns, and standard lift-off is then employed to define the metallization layer. This metallization layer connects to the larger aforementioned lead-frame, and also serves as a mask for the subsequent etching process. The metal-masked SiC epilayer is etched in an Ar/NF_3 plasma created by an electron cyclotron resonance (ECR) plasma-etching system. This dry etch step removes the SiC in unprotected regions and undercuts the silicon beneath the masked SiC, to result in a fully

suspended NEMS beam[17]. The completed devices, such as depicted in Figure S2, are geometrically characterized by a scanning electron microscope (SEM).

The NEMS mass sensor used in these measurements is a 100nm thick, doubly-clamped silicon carbide beam ~1.7μm long, ~120nm wide. In addition to its function as an etch mask, the topmost, thin-film metallization layer subsequently enables sensitive and well-validated magnetomotive actuation and transduction[18].

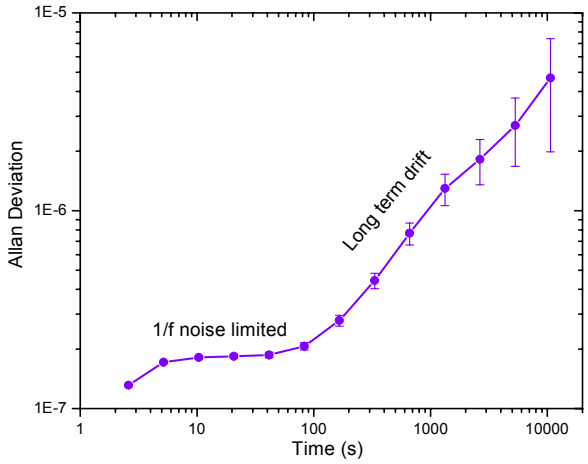

Figure S3. *Allan deviation of a typical NEMS resonator used in this work, as a function of integration time. The device is phase locked within a control circuit to sustain its fundamental vibrational mode at ~450 MHz.*

NEMS Mass Sensor Characterization

Data presented in this work are obtained with devices such as described previously, which flexurally vibrate in-plane, with a typical fundamental mode resonance at ~450MHz and quality factor of ~2000. A typical response curve is shown in Figure S2 (panel c).

Prior to embedding candidate devices in the UHF phase locked loop (PLL) circuitry each is fully characterized electromechanically, in vacuum. This involves immersion in, typically, a 7T magnetic field and execution of the RF drive frequency sweeps with a network analyzer to locate the various NEMS electromechanical resonances. Each resonant mode observed is verified to be electromechanical in nature by confirming its expected dependence upon magnetic field ($\propto B^2$) and drive power, which is taken well into the non-linear mechanical regime[19].

The temperature dependence of the fundamental-mode resonance is characterized by sweeping the sample stage temperature slowly from 25K to 65K, while recording the NEMS frequency. The resulting curve has an inverted-"U" shaped curve. We find that in the temperature range between 35K and 40K the NEMS fundamental resonance frequency is least sensitive to the temperature changes. This reduced temperature coefficient is an additional motivation for our operation at 40K; in this regime we have verified that thermal fluctuations and thermalization of landing proteins have negligible effect on the NEMS resonant frequency.

RF characterization

To determine the temporal stability of the phase locked loop we run the system in closed loop for extended time periods and determine the resulting Allan deviation. Figure S3 shows a typical plot of Allan deviation versus measurement integration time. In the flat region between 3-30 seconds the Allan deviation is limited by the *1/f* noise. For longer measurement times drift becomes the major source of instability; for shorter times white noise dominates.

NEMS Mass Responsivity

The dynamics of a flexural mode NEMS resonator can be modeled as a simple damped harmonic oscillator[20]. Referring to the coordinate system introduced in Figure 2 in the main text and

DOI: 10.1038/NNANO.2009.152

$$P.E. = \frac{1}{2} k y_{center}^2 \quad , \quad K.E. = \frac{1}{2} M_{eff} \dot{y}_{center}^2 \quad ,$$

$$f_{nems} = \frac{1}{2\pi} \sqrt{\frac{k}{M_{eff}}}$$

Here y_{center} denotes the center-of-beam displacement, k denotes the modal stiffness coefficient, and M_{eff} denotes the modal mass of the fundamental mode, f_{nems} is the resonance frequency of the flexural mode.

At this point, it is illuminating to show how modal mass can be calculated. The mechanical resonator oscillating with a certain amplitude, $y(t)$, and angular frequency, ω, possesses kinetic energy. This kinetic energy can be calculated by considering infinitesimal slices of material along the length of the beam and summing up their infinitesimal kinetic energies:

$$K.E. = \frac{1}{2} \int dm\, \dot{y}^2 = \frac{1}{2} \int_{x=0}^{x=L} \rho A\, dx\, [\dot{y}(x)]^2$$

Here dm is the mass of the each infinitesimal slice considered, y is the displacement of the beam at that point, ρ is the mass density, A is the cross section of the beam and L is its length.

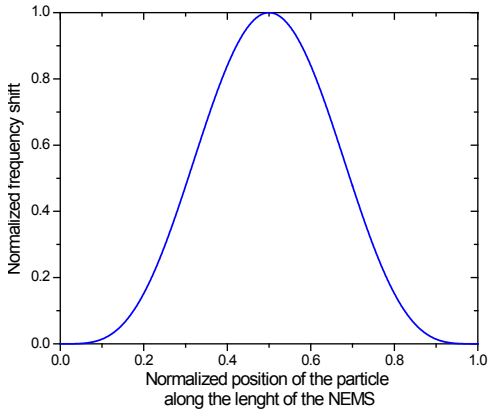

***Figure S4**: The position dependent responsivity of the doubly-clamped NEMS resonator for the fundamental mode. The observed frequency shift is maximized when the particle adsorbs at the center of the beam. Minimal shifts are induced for adsorption near the clamping points.*

The displacement at a point x along the beam can be expressed as: $y(x) = y_{center} \times \varphi(x)$, where $\varphi(x)$ is the mode shape. Using this relationship:

$$K.E. = \frac{1}{2} \int_{x=0}^{x=L} \rho A dx\, [\dot{y}_{center} \times \varphi(x)]^2 = \frac{1}{2} \left[\rho A L\, \frac{1}{L} \int_{x=0}^{x=L} [\varphi(x)]^2 dx \right] \dot{y}_{center}^2$$

The expression inside the large square brackets is the modal mass, M_{eff}. For point mass loading of a doubly clamped beam the effective mass is given by [21],

$$M_{eff} = M_{total} \times \frac{1}{L} \int_{x=0}^{x=L} [\varphi(x)]^2\, dx = 0.397\, M_{total}$$

When a point mass, δm, is added to the resonator, at a point x' along the beam, the total kinetic energy carried by the resonator will change, as the added mass is forced to oscillate with the beam. The new kinetic energy is given as:

$$K.E. = \frac{1}{2} M_{eff} \dot{y}_{center}^2 + \frac{1}{2} \delta m\, [\dot{y}(x')]^2$$

Using $y(x') = y_{center} \times \varphi(x')$, the above equation translates into:

$$K.E. = \frac{1}{2} M_{eff} \dot{y}_{center}^2 + \frac{1}{2} \delta m\, \dot{y}_{center}^2\, [\varphi(x')]^2 = \frac{1}{2} \left[M_{eff} + \delta m [\varphi(x')]^2 \right] \times \dot{y}_{center}^2$$

Thus, the resonator's effective mass is changed to $M_{eff} + \delta m[\varphi(x')]^2$. This in turn changes the resonance frequency:

$$f'_{nems} = \frac{1}{2\pi}\sqrt{\frac{k}{M_{eff} + \delta m[\varphi(x')]^2}}$$

For $M_{eff} \gg \delta m$, as in our experiment, one can make a Taylor expansion of the square bracket to arrive at the frequency shift caused by the added mass:

$$\Delta f = f_{nems} - f'_{nems} = \left\{-\frac{1}{2}\frac{f_{nems}}{M_{eff}}[\varphi(x')]^2\right\}\delta m$$

The expression in the curly bracket is the position-dependent responsivity of NEMS:

$$\Re \equiv \frac{\delta f}{\delta M} = -\frac{f_{\text{nems}}}{2\,M_{eff}}[\varphi(x')]^2$$

The shape of the position dependent responsivity is shown in figure S4.

As an example, we now calculate the responsivity for a point particle landing at the center of the beam. For this case $\varphi(x') = 1$.

The NEMS beam used in the experiment is 1.7 µm long, 120 nm wide and containing three layers: 100 nm SiC (ρ=3.2 g/cm^3), 40 nm Al (ρ = 2.7 g/cm^3), and 5 nm Ti (ρ=4.5 g/cm^3)

Thus:

M_{total} =92 10^{-15}g = 92 fg

and

$$\Re = -\frac{f_{\text{nems}}}{2\,M_{eff}} = 6.2\,\frac{Hz}{zg}.$$

The experimentally observed mass responsivity of 12 *Hz/zg* is reasonably close to this calculated value.

Based on the experimentally-measured mass responsivity, we deduce that mass of the beam to be M_{total}=*46fg*. Using this experimentally-observed total mass, and an *upper* bound to our typical Allan deviation, $\sigma_A(\sim 5sec) \sim 3.5 \times 10^{-7}$, we deduce the following upper bounds to our mass sensitivity δM and the frequency instability for these experiments[2]:

$$\delta M = 2\sqrt{2}M_{eff}\sigma_A(\tau) \sim 10kDa$$

$$\delta f = \delta M/(2M_{eff})f_{\text{nems}} \sim 250Hz$$

DOI: 10.1038/NNANO.2009.152

Control runs

To verify that the change in resonant frequency of the NEMS is due to mass loading from protein molecules or nanoparticles landing on the NEMS, we perform the following three distinct control runs while tracking the resonant frequency of the NEMS:

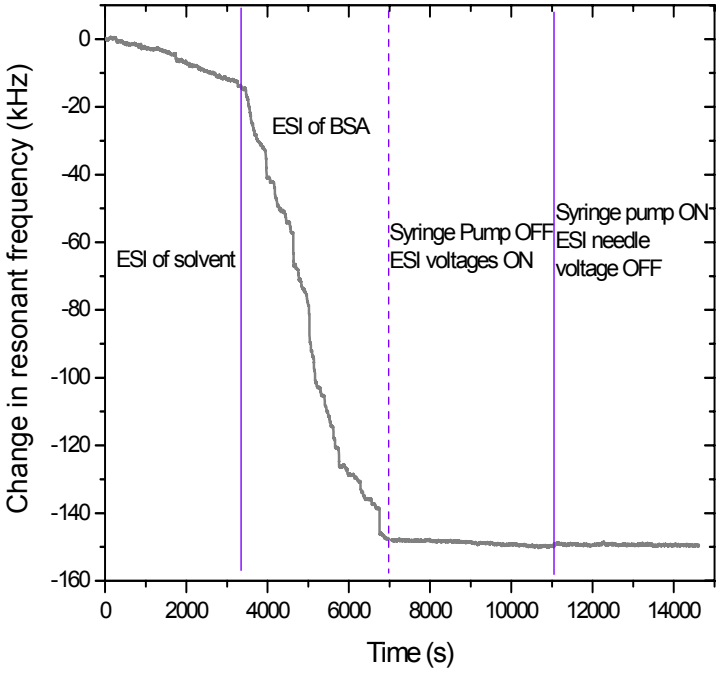

***Figure S5**: The response of the NEMS frequency during the control runs and the ESI of BSA.*

1. Turn off the syringe pump delivering the protein solution to the ESI needle. Keep all ESI voltages and ion optics control voltages on. Proteins do not reach the ESI needle, hence protein ions should not be produced (beyond rare events arising from the dislodging of sparse protein residue accumulated within the needle, etc. – *i.e.* from previous NEMS-MS runs.
2. Turn off the ESI needle voltage. All the other parameters are kept the same as for ESI injection during regular NEMS-MS operations. In this case although the protein solution is ejected from the ESI needle due to the flow pressure generated by the syringe pump and the nebulising gas flow, the resulting droplets are not charged and any proteins, if produced, will not be transported to the NEMS by the ion guide.
3. Run the ESI with the clean solvent devoid of analytes. Assuming that there are no leftover proteins in the ESI system (as described in #1 above) we should see minimal change in the resonant frequency of the NEMS.

Figure S5 shows one such time record of the resonant frequency of the NEMS during the ESI of Bovine Serum Albumin (66kDa) and three different control runs. The resonant frequency of the NEMS changes radically during the ESI of BSA protein. The frequency change is composed of scores of frequency jumps similar to the ones shown in Figure 2. During the control runs, however, the total change in resonant frequency is noticeably smaller. This indicates that the mass loading indeed arises from the protein ions produced during ESI. We believe the mass loading of the NEMS during solvent-only ESI is largely due to proteins remaining in the ESI system from previous runs. The resonant frequency changes during the other two control runs are minimal and compare well with the frequency fluctuations observed due to background gas molecules.

Cross-checks: ensuring that frequency-shift "events" indeed arise from nanoparticle/protein adsorption

One distinguishing feature of the ESI process is that it typically produces species with mass-to-charge ratios of order *m/z* ~1000. This can be easily verified in our experiments. Based on the relative cross-sectional area of the faraday cup and the NEMS, and using the charge-to-mass transformation, we can deduce the expected frequency shift due to mass loading of the NEMS convert from the current observed at Faraday cup. Figure S6 shows the frequency change of the NEMS due to mass loading and the expected frequency change assuming several different average *m/z* values.

Adsorption-event curve-fitting analysis

In order to construct frequency-shift histograms from the experimental time records of resonance frequency while under phase-lock, one needs an objective method to identify adsorption events and measure the magnitude of their corresponding frequency shifts, Δf . We have developed a Matlab script to serve this purpose. The experimental time records consist of scores of discrete frequency jumps. We characterize each of these jumps by the maximum slope at the jump center and zero slopes at the edges. Our Matlab routine scans the experimental data for local regions of high slope, subject to the conditions that our frequency-shift threshold is set to be $\Delta f \geq 2 \times \delta f$, records the experimental data as a frequency step. (As described in the main text, δf is the frequency resolution). By these procedures the extracted frequency jumps are "filtered" to reject both impulsive noise spikes and long term drifts. Practically, this is achieved by putting lower and upper limits on the acceptable time-scale of "real" frequency jumps. Later, each frequency jump data in this filtered set is fitted to the modeled time-response of the PLL circuitry as described in the main text. The parameters in this PLL model are chosen initially from circuit analysis and validated by separate measurements. These circuit parameters are iteratively varied slightly to obtain the best fit between the experimental characterization measurements and calculated PLL temporal response function (see main text, Figure 2b). The heights of the frequency jumps obtained during the fitting process are

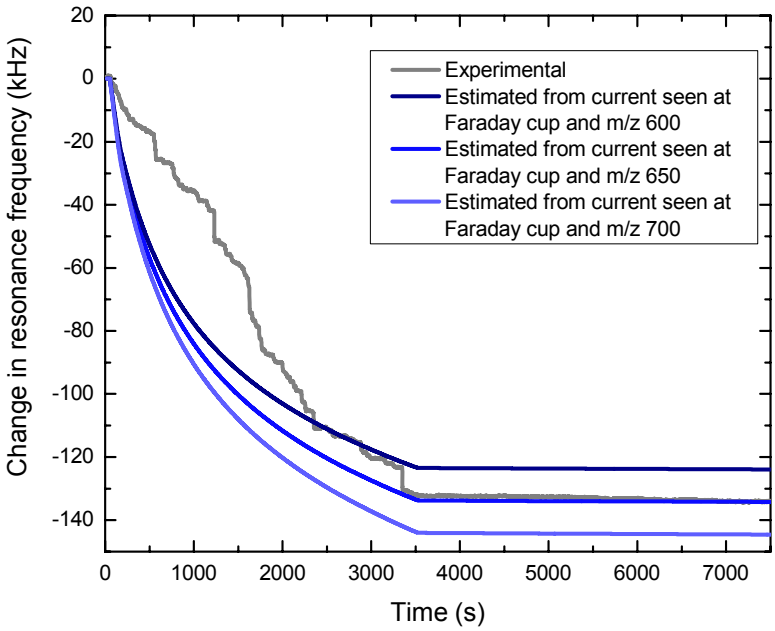

Figure S6. *The frequency change observed during the experiment (gray solid line) and the frequency change expected based on the ionic current measured at the faraday cup. The expected curve is calculated by assuming an average m/z of 600, 650 and 700 and converting it into mass deposited on the NEMS.*

DOI: 10.1038/NNANO.2009.152

recorded and used to construct the experimental event-probability histograms.

Histograms during "analysis" and "control" runs

Each NEMS-MS protein or nanoparticle analysis run is followed by a control run of roughly the same time scale. During these control runs the syringe pump is shut off and all other controls of the system are maintained as during the corresponding analysis run. Due to the frequency-fluctuation noise of the phase-locked NEMS, a finite number of abrupt frequency jumps will be counted even during the control run. We generate separate histograms of the jumps obtained during the analysis runs and the control runs. Typical histograms for the analysis and the control runs from NEMS-MS for BSA are shown in figure S7. The histograms from control runs are then used to perform background subtraction from the histogram obtained from the corresponding analysis runs.

Calculation of the ion transmission transfer function for the hexapole ion guides.

To determine the efficiency of ion transmission from the ESI source to the NEMS as a function of mass/charge ratio we numerically simulated the transmission properties of our system (using the SIMION software). The results of the simulations for three different hexapole frequencies are shown in figure S8.

With the hexapole operating at a frequency of 1.1 MHz, the ion optics of our system favor the transmission of ions with *m/z* in the range from 100 to 1000, while for a lower hexapole frequency (450kHz) they favor transmission of ions with larger *m/z* (see figure S8). During the positive ESI process used for proteins, protonation occurs at the basic residue sites of the proteins. The resulting *m/z* spectra tend to be bell shaped curves, and the maximum charging state observed is consistent with the number of basic residues expected for small proteins[22,23]. However, for large proteins (similar to the ones used in our experiments), as the number of charges accumulated increases, Columbic repulsion prevents basic residue sites from acquiring additional charge[24]. Furthermore, for larger proteins the basic amino acids buried within the protein structure tend to be inaccessible to the more acidic liquid and/or gas phase molecules. Thus larger proteins generally have larger m/z values.

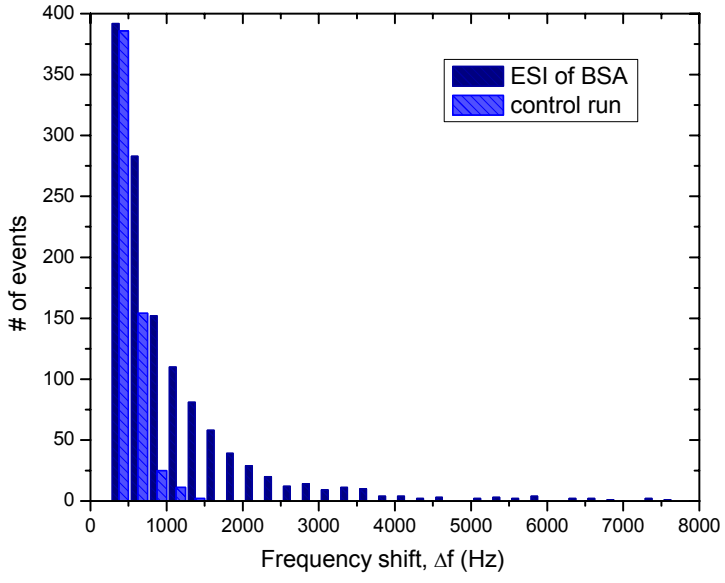

Figure S7: *The histogram obtained during the ESI of BSA and the control run of the experiment. The frequency jumps recorded during the control run are primarily due to the measurement noise and drop off rapidly at higher frequencies.*

We can easily verify the above

hypothesis by obtaining the frequency shift histograms for β-amylase with hexapole operating at frequencies 1.1 MHz and repeating the experiments with 450 kHz. Based on SIMION simulations, we expect that the higher hexapole frequency would preferentially transmit ions with low *m/z* and hence of lower mass. This would translate into a larger low frequency peak at a higher hexapole frequency. The experimental results are shown in figure S9. Note that the probability of observing a low mass (Δf <1.5 kHz) event is dramatically reduced when the hexapole frequency is changed from 1.1 MHz to 450 kHz. In addition, the probability of observing larger frequency shifts (larger mass) is also significantly improved at 450 kHz.

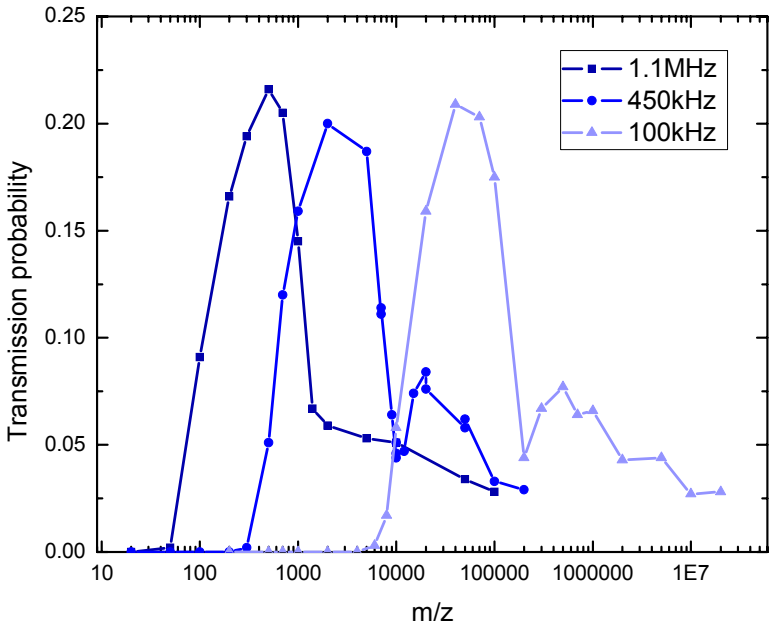

Figure S8. *Transmission probability of the ions through the ion optics. The plot clearly shows the preference for low m/z transmission with higher hexapole frequency.*

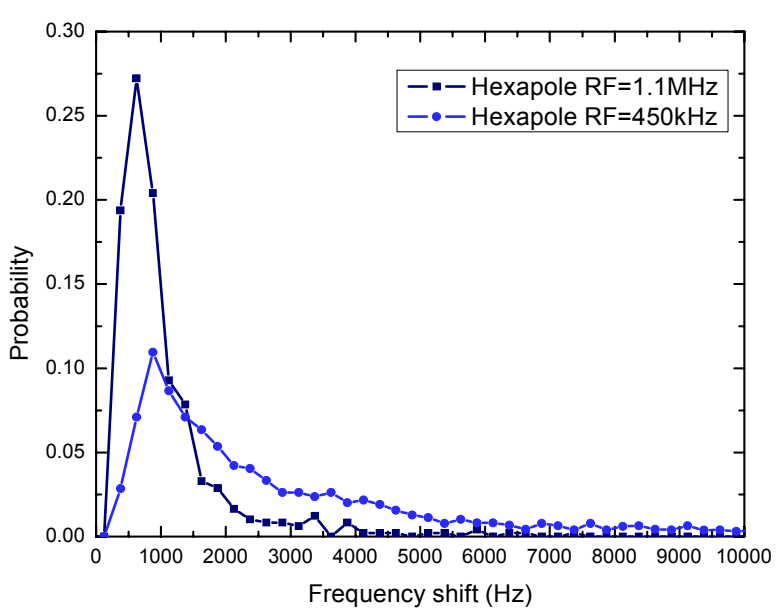

Figure S9. *Plot of probability of frequency shifts during electrospray ionization of β-Amylase. Notice the dramatic change in the relative heights at low frequency. This indicates that the hexapole RF frequency of 1.1 MHz favors the transmission of low mass ions. Also visible are the shoulder at about 3.5kHz corresponding to β-Amylase monomers landing close to the center of the NEMS.*

NEMS-MS of β-amylase

We show results from one additional NEMS-MS experiment on a protein sample. Figure S10 shows the results obtained from ESI of β-amylase with a hexapole drive frequency of 450 kHz. The event probability histogram displays a broad peak at 3600Hz, which we associate with the β-amylase monomer. Sweet potato β-amylase is known to be a tetramer of identical subunits[25] and under a variety of experimental conditions the protein molecules can fragment into

DOI: 10.1038/NNANO.2009.152

individual subunits[26]. We believe the broadening of the monomer peak, as well as the absence of a clear bicuspid shape in the histogram, arise from the presence of such protein subunits in these experiments. As shown by the curve "decomposition" in Figure S10, the experimental histogram can be readily explained by assuming a weighted superposition of subunits.

Data analysis procedure used to construct first-generation NEMS-MS spectra.

To provide an unbiased extraction of our first NEMS-MS mass spectra from the experimentally obtained event-probability histograms, we fit the experimental data to realistic models. These models are based on predicted NEMS-MS event-probabilities assuming the injection of multicomponent mixtures – in these experiments, sample solutions containing either a Au nanoparticle dispersion, a family of BSA oligomers, or a family of re-aggregated β-amylase subunits. These fits are provided in an unbiased manner through automated procedures that allow the relative intensities of the sample's components to be deduced. We treat the intensities of the solution components as variable parameters, and use the minima of the sum-of-squared-errors (SSE) to determine the relative intensities of the (variable-radius) nanoparticles or molecular species that adsorb upon the NEMS. We now describe the specific examples presented in this initial NEMS-MS work.

Calculation of the SSE

Gold: We generate a theoretical histogram from 1 million adsorption events. This histogram assumes a normalized mass of 1 for the nanoparticle and includes the effect of our finite, 250Hz frequency resolution. We vary the mean radius of the gold nanoparticles in steps of 0.01nm from 1.9nm to 2.9 nm and the standard deviation in steps of 0.003nm from 0.2nm to 0.75nm. Theoretical histograms are generated by "rescaling" the master histogram for each value of the mean radius and the standard deviation. Each theoretical histogram is then compared against the experimental histogram to calculate the SSE for each specific radius/deviation value. The contour map of Figure 3c (main text) represents the SSE's determined in this manner.

BSA: A theoretical histogram of 100,000 events is generated similar to the one for the gold. In this case we assume that the protein solution is composed of five oligomers: monomers, dimers, trimers, tetramers, and pentamers. We adjust the fractional intensities of the monomer, dimer, trimer and pentamer event probability in steps of 0.01 and calculate the resulting SSE between the resulting theoretical histogram and the data. Fine adjustments of the tetramer value, the weakest peak in the experimental curve, are carried out to maintain the total weight of unity. We weight the SSE to suppress the effect of the freq shifts < 500Hz which are deemed experimentally unreliable (as these are heavily biased by NEMS frequency-fluctuation noise; see main text for discussion.) For each set of oligamer probabilities, we "rescale" the calculated histogram and compare it with the experimental histogram to calculate the SSE. On the next page Figure S11 shows the fit residues from the ten two-dimensional cuts through the five-dimensional SSE optimization space.

β-Amylase: A theoretical histogram of 100,000 events is generated, similar to the one for the gold. In this case we assume that the protein is composed of monomer and the other four of its first five re-aggregated subunits. The subunits themselves can aggregate to form particles of higher mass. Here we change the monomer and subunit event probabilities in steps of 0.02. As for BSA, the SSE in this case are weighted to reduce the effect of the freq shifts < 500Hz. As for the previous examples each set of probabilities for the oligomers, we "rescale" the histogram and compare it with the experimental histogram to calculate the SSE. A graphical representation of this optimization process, not shown here, is similar in appearance to Figure S11.

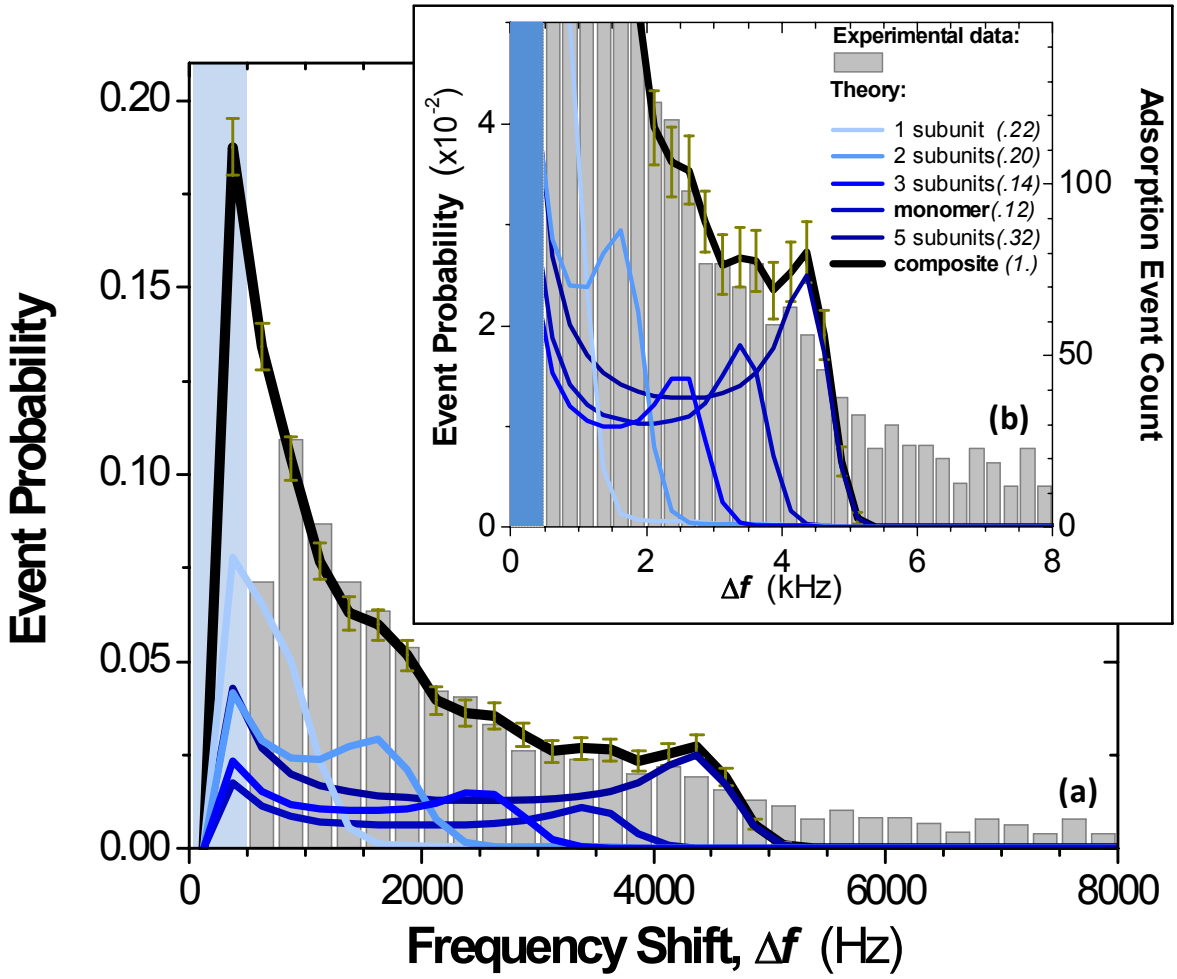

Figure S10. NEMS-MS of β-Amylase by adsorption-event probability analysis. *Discrete experimental adsorption events, obtained using a hexapole drive frequency of 450 kHz, are assigned to 250 Hz wide bins in this histogram (grey bars), as done for BSA as described in the main text.* ***(a)*** *Expanded view of the low event probability region. The experimental histogram can be readily explained by assuming a weighted superposition of subunits. A clearly-detailed theoretical decomposition (colored curves) of the composite curve (black trace) is shown. A broad shoulder is evident in the event probability histogram at 3600Hz; we associate this with β-amylase monomer. The low, but finite probability in the experimental data for Δf >5kHz appears to indicate the presence of compound species with masses greater than that of five protein subunits, which we make no attempt to modeled in our composite curve.* ***(b)*** *Overall view of the entire data set and composite curves. The weighting functions for the composite curve, here determined using residual method discussed in the text, are displayed.*

DOI: 10.1038/NNANO.2009.152

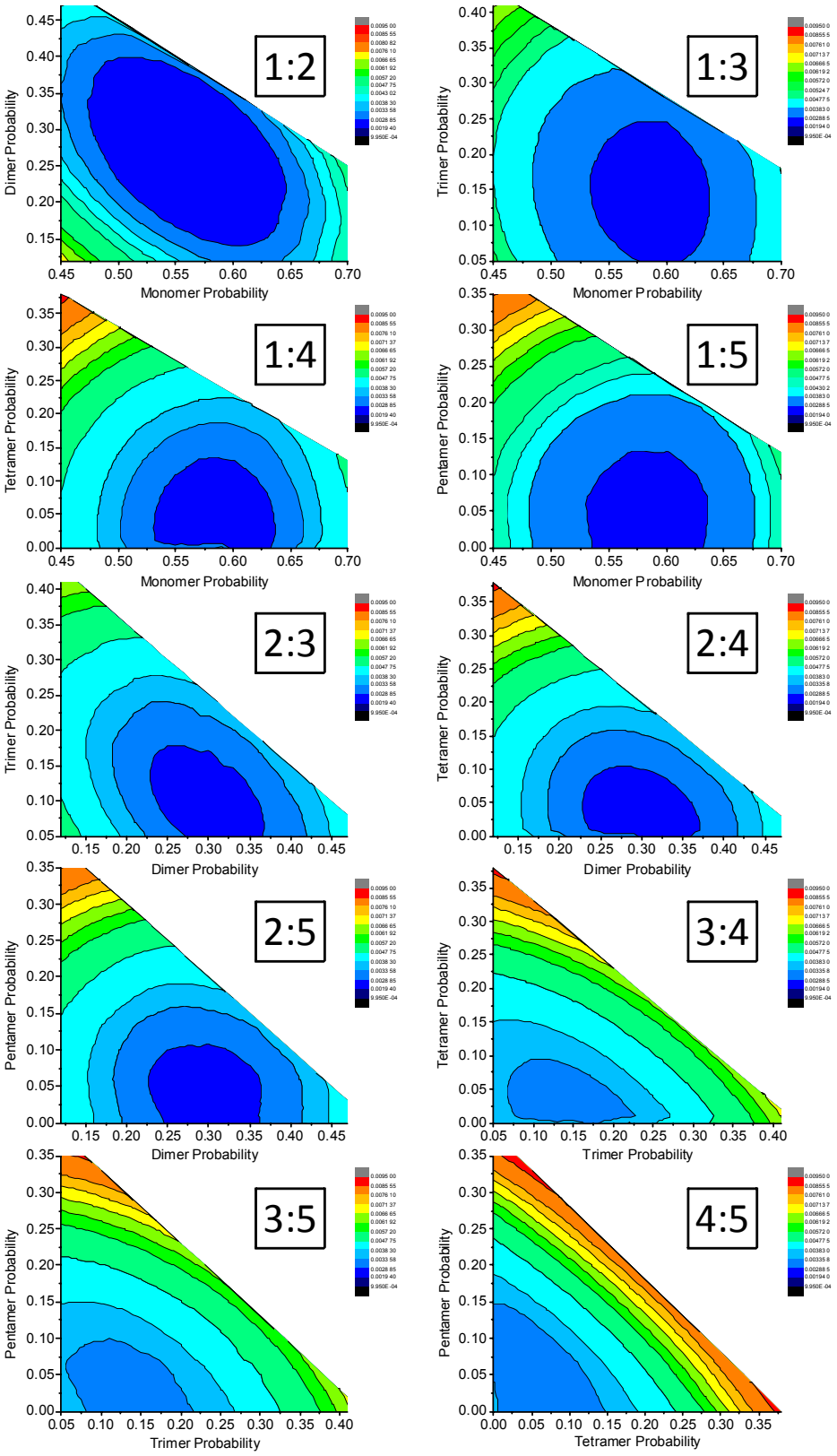

Figure S11. Optimization of weighting coefficients for mass spectrum of BSA and its oligomers. *Each subplot shows the variation of the SSE as we vary the event probability of the various oligomers. Note that the optimization was obtained by varying the probability of all the oligomers. The plots are two dimensional snapshots of the entire optimization process.*

Analysis of BSA and β-Amylase assuming presence of single species:

As an alternative procedure to the analyses of protein described above, where the presence of multiple species has been assumed, we also have analyzed our experimentally-obtained histograms by assuming that only a single mass species is present in solution. We then compare the resulting theoretical histogram with the experimental histogram to obtain the SSE, and carry out this procedure for a range of analyte mass. As seen in figure S12, the SSE shows a minumum for a mass of approximately 95kDa for BSA. This is fairly close to the average mass value of 118kDa obtained by summing the weighted average of the intensities obtained in Figure 4.

A similar analysis of β-Amylase gives a SSE minimum at ~250kDa. The minimum for this protein is rather shallow, hence mass determination by this approach is less conclusive.

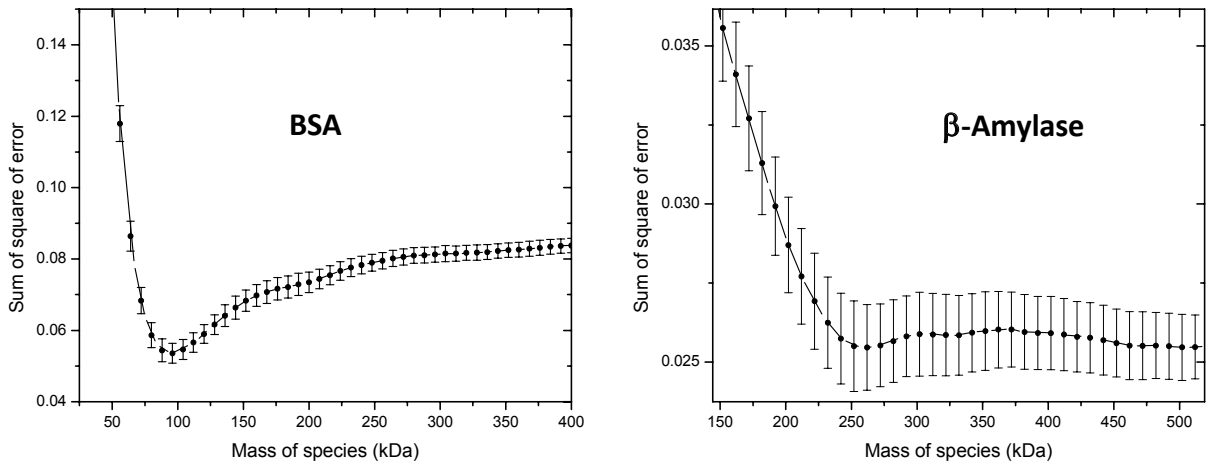

Figure S12. Residue plot obtained for BSA and β-Amylase. *The experimental histograms were compared with theoretical histogram obtained by assuming the presence of only a single mass species. The error bars are due to the statistical fluctuation of the theoretical histogram.*

Native gel electrophoresis of BSA

There is significant precedent for the high degree of multimerization in the NEMS-MS spectra we observe. This has been previously elucidated in studies of non-covalent interactions using ESI-MS[27-30]. Indeed, in Ref. 29 the same BSA monomer-to-dimer ratio of 2:1, as deduced from our NEMS-MS method, was previously observed.

To further confirm high multimer content in our samples, we have analyzed our BSA sample solution by performing native polyacrylamide gel electrophoresis (native PAGE). Figure S13 shows native PAGE gels of different BSA samples performed at NINT (Edmonton) and at Caltech. The Caltech BSA sample is from the same lyophilized powder used in the NEMS-MS experiment and prepared at the same molarity. Both samples show several distinct bands that

DOI: 10.1038/NNANO.2009.152

likely correspond to different multimers of BSA with the rightmost band being the monomer. Note that the density in the multimer bands is a significant fraction of the total density. This appears to imply that there is a rather high degree of multimerization.

However, two points of caution should be noted: (i) Native PAGE cannot provide a direct, straightforward connection between the observed electrophoretic mobility and mass; many additional factors contribute to analyte mobility. (ii) The ESI process parameters employed in our experiments themselves can alter the degree of species aggregation; hence this can be different than that of the condensed state in fluid. Hence, we view these results of the native PAGE as corroborating, but not proving, that a high degree of multimerization exists in our sample solution.

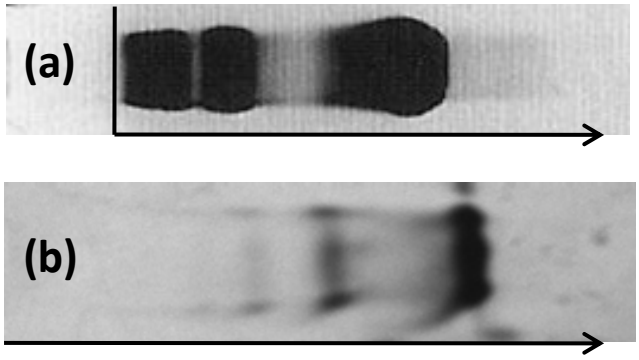

Figure S13. Native PAGE of BSA. *The migration direction is to the right (indicated by the arrows). Molecules of larger hydrodynamic size and lower charge have lower mobility.* ***(a)*** *NINT sample. The 3 broad bands may correspond to (from right to left, the monomer, dimer, and trimer of BSA. The bands may hide additional components, particularly the leftmost band, which extends right to the starting edge of the gel.* ***(b)*** *Caltech sample. Four bands are visible and may correspond to the monomer through tetramer of BSA (from right to left). In both cases (a) and (b), there is substantial weighting on the higher multimer content.*

References:

1 Ekinci, K.L., Huang, X.M.H., & Roukes, M.L., Ultrasensitive nanoelectromechanical mass detection. *Appl. Phys. Lett.* **84,** 4469-4471 (2004).

2 Feng, X.L., Ph.D. Dissertation, California Institute of Technology, 2006.

3 Feng, X.L., White, C.J., Hajimiri, A., & Roukes, M.L., A self-sustaining ultrahigh-frequency nanoelectromechanical oscillator. *Nature Nanotech.* **3,** 342-346 (2008).

4 Yang, Y.T., Callegari, C., Feng, X.L., Ekinci, K.L., & Roukes, M.L., Zeptogram-scale nanomechanical mass sensing. *Nano Lett.* **6,** 583-586 (2006).

5 Yamashita, M. & Fenn, J.B., Electrospray ion source. Another variation on the free-jet theme. *J. Phys. Chem.* **88,** 4451-4459 (1984).

6 Fenn, J.B., Mann, M., Meng, C.K., Wong, S.F., & Whitehouse, C.M., Electrospray ionization for mass spectrometry of large biomolecules. *Science* **246,** 64-71 (1989).

7 Dass, C., *Fundamentals of Contemporary Mass Spectrometry*. (Wiley-Interscience, 2007).

8 Douglas, D.J. & French, J.B., Collisional focusing effects in radio frequency quadrupoles. *J. Am. Soc. Mass. Spectrom.* **3,** 398-408 (1992).

9 Chernushevich, I.V. & Thomson, B.A., Collisional Cooling of Large Ions in Electrospray Mass Spectrometry. *Anal. Chem.* **76,** 1754-1760 (2004).

10 Kantrowitz, A. & Grey, J., A High Intensity Source for the Molecular Beam. Part I. Theoretical. *Rev. Sci. Instrum.* **22,** 328-332 (1951).

11 Whitehouse, C.M., Dreyer, R.N., Yamashita, M., & Fenn, J.B., Electrospray interface for liquid chromatographs and mass spectrometers. *Anal. Chem.* **57,** 675-679 (1985).

12 Lebrilla, C.B., Amster, I.J., & McIver, R.T., External ion source FTMS instrument for analysis of high mass ions. *Int. J. Mass Spectrom. Ion Processes* **87,** R7-R13 (1989).

13 Mciver Jr., R.T., United States Patent No. ***4535235*** (1985).

14 Ronald, M.J. & Scott, L.A., Simplified radio-frequency generator for driving ion guides, traps, and other capacitive loads. *Rev. Sci. Instrum.* **71,** 4335-4337 (2000).

15 Ronald, M.J., Dieter, G., & Scott, L.A., Simple radio-frequency power source for ion guides and ion traps. *Rev. Sci. Instrum.* **68,** 3357-3362 (1997).

16 Zorman, C.A. *et al.*, Epitaxial growth of 3C--SiC films on 4 in. diam (100) silicon wafers by atmospheric pressure chemical vapor deposition. *J. Appl. Phys.* **78,** 5136-5138 (1995).

17 Yang, Y.T. *et al.*, Monocrystalline silicon carbide nanoelectromechanical systems. *Appl. Phys. Lett.* **78,** 162-164 (2001).

18 Cleland, A.N. & Roukes, M.L., Fabrication of high frequency nanometer scale mechanical resonators from bulk Si crystals. *Appl. Phys. Lett.* **69,** 2653-2655 (1996).

19 Postma, H.W.C., Kozinsky, I., Husain, A., & Roukes, M.L., Dynamic range of nanotube- and nanowire-based electromechanical systems. *Appl. Phys. Lett.* **86,** 223105-223103 (2005).

20 Cleland, A.N., *Foundations of Nanomechanics: From Solid-State Theory to Device Applications*. (Springer Verlag, 2002).

21 Karabacak, D.M., Ph.D. Dissertation, Boston University, 2008.

22 Covey, T.R., Bonner, R.F., Shushan, B.I., Henion, J., & Boyd, R.K., The determination of protein, oligonucleotide and peptide molecular weights by ion-spray mass spectrometry. *Rapid Commun. Mass Spectrom.* **2,** 249-256 (1988).

23 Smith, R.D., Loo, J.A., Edmonds, C.G., Barinaga, C.J., & Udseth, H.R., New developments in biochemical mass spectrometry: Electrospray ionization. *Analytical Chemistry (Washington) ; Vol/Issue: 62:9; DOE Project*, Pages: 882-899 (1990).

24 Loo, J.A. & Loo, R.R.O., *Electrospray Ionization Mass Spectrometry of Peptides and Proteins*. (John Wiley & Sons 1997).

25 Cheom Gil Cheong *et al.*, Crystallization, molecular replacement solution, and refinement of tetrameric beta-amylase from sweet potato. *Proteins: Struct., Funct., Genet.* **21,** 105-117 (1995).

26 Justin L. P. Benesch, Brandon T. Ruotolo, Douglas A. Simmons, & Robinson, C.V., Protein Complexes in the Gas Phase: Technology for Structural Genomics and Proteomics. *ChemInform* **38** (2007).

27 Light-Wahl, K.J., Schwartz, B.L., & Smith, R.D., Observation of the Noncovalent Quaternary Associations of Proteins by Electrospray Ionization Mass Spectrometry. *JACS* **116,** 5271-5278 (1994).

28 Joseph A. Loo, Observation of large subunit protein complexes by electrospray ionization mass spectrometry. *J. Mass Spectrom.* **30,** 180-183 (1995).

29 Yang Wang, M.S., Arnd Ingendoh, Jochen Franzen,, Analysis of non-covalent protein complexes up to 290 kDa using electrospray ionization and ion trap mass spectrometry. *Rapid Commun. Mass Spectrom.* **14,** 12-17 (2000).

30 Loo, J.A., Electrospray ionization mass spectrometry: a technology for studying noncovalent macromolecular complexes. *Int. J. Mass Spectrom.* **200,** 175-186 (2000).